Near-surface characterization using shear-wave resonances: A case study from offshore Svalbard, Norway

Kittinat Taweesintananon[*,†,‡,‖], Robin André Rørstadbotnen[*,†], Martin Landrø[*,†], Ståle Emil Johansen[†,§], Børge Arntsen[†,§], Matthias Forwick[¶], and Alfred Hanssen[¶]

[*] *Acoustics Group, Department of Electronic Systems, NTNU – Norwegian University of Science and Technology, Trondheim 7491, Norway.*

[†] *Centre for Geophysical Forecasting, NTNU – Norwegian University of Science and Technology, Trondheim 7491, Norway.*

[‡] *PTT Exploration and Production Public Company Limited (PTTEP), Bangkok 10900, Thailand.*

[§] *Department of Geoscience and Petroleum, NTNU – Norwegian University of Science and Technology, Trondheim 7031, Norway.*

[¶] *Department of Geosciences, UiT The Arctic University of Norway, Tromsø 9037, Norway.*

[‖] *Corresponding author: Kittinat Taweesintananon (E-mail: kittinatt@pttep.com)*

(April 5, 2024)

GEO-2023-0530.R2.accepted

Running head: **S-wave resonances for near-surface imaging**

ABSTRACT

Shear-wave (S-wave) resonances are typically observed when the surficial marine sediments over a rock substrate have relatively low S-wave velocities. We observe these phenomena using ocean-bottom fiber-optic distributed acoustic sensing (DAS) in two subsea fiber-optic telecommunication cables in Svalbard, Norway. Strong seismic energy from sufficiently large earthquakes is required to trigger and enhance the multiple order modes of S-wave resonances. Here, we use the interpreted S-wave resonance frequencies of the first two modes to determine the thickness and the S-wave velocity of the near-surface low-velocity layer (LVL) beneath the seafloor. Additionally, we use existing active P-wave seismic reflection data to determine the LVL thickness and to help build a more accurate S-wave velocity model from the S-wave resonance frequencies. The estimated S-wave velocity varies laterally within the LVL formation. Here, we find that the sediments or deposits with high S-wave velocity presented in the estimated LVL model agree with the distribution of some glacigenic sediments and landforms deposited in the survey area. Therefore, S-wave resonances measured by ocean-bottom DAS can be used to characterize the corresponding near-surface LVLs.

INTRODUCTION

Near-surface geologic structures can be imaged or mapped by active and passive seismic methods. P-wave seismic reflection surveying is currently the most common and effective method for subsurface exploration. It is an active seismic method, in which the human-controlled seismic energy sources are required to obtain a reliable seismic image of the subsurface. In addition, passive seismic methods have been proposed to reduce operational cost and time associated with human resources. Such methods include the ambient noise analysis of surface waves (Foti et al., 2018) or seismic reflections (Draganov et al., 2009). In this paper, we explore an alternative passive seismic method based on shear-wave (S-wave) resonances in the subsurface using ocean-bottom fiber-optic distributed acoustic sensing (DAS).

DAS is a technology that can exploit an optical fiber in standard telecommunication cables as an extended spatial array of acoustic sensors (Hartog, 2017). Many optical fibers in these cables are not used for telecommunication. Therefore, it is possible to repurpose these unused "dark" fibers to serve as ocean-bottom distributed acoustic sensors to measure, among other signals, dynamic strains that are caused by ocean-bottom pressure fluctuations. Moreover, recent research shows that it is possible to perform high-speed optical communication and distributed vibration sensing concurrently in an optical fiber (He et al., 2023). Such a scheme of using shared spectrum in communication and distributed fiber-optic sensing offers the possibility of using DAS in any existing fiber-optic telecommunication cable.

DAS measures the strain fluctuations at each sensing element of an optical fiber.

A DAS interrogator can measure the strain data along the fiber up to 171 km length in a controlled experiment (Waagaard et al., 2021). When the fiber is deployed in the field for practical uses, the noise floor detrimentally increases in the recording channels beyond 90–100 km length, such that the maximum length typically decreases to approximately 140–150 km depending on the quality of the fiber. In addition, DAS can measure the data with a spatial sampling interval as small as 1 m, which creates arrays of tens of thousands of sensors at relatively low cost.

DAS in subsea fiber-optic telecommunication cables can measure the loading pressure fluctuations at the ocean bottom originating from a variety of sources (Landrø et al., 2022). It can detect ocean surface gravity waves (OSGWs), microseisms and earthquakes (Lindsey et al., 2019; Sladen et al., 2019). Williams et al. (2019) demonstrate that ocean-bottom DAS can record the seismic waves from a distant earthquake, OSGWs, and Scholte waves. In addition, Taweesintananon et al. (2023) use ocean-bottom DAS to record the loading pressure response associated with the ocean swells propagating from distant storms and to record the S-wave resonances in near-surface low-velocity layers (LVLs), i.e., soft marine sediments.

Underwater interface wave analysis is commonly used to estimate a 1D S-wave velocity model of soft marine sediments from the Scholte interface wave dispersion curve in the f-v spectra (Dong et al., 2021). For example, Dong et al. (2013) demonstrate this application using the seabed seismic data generated from an S-wave source. Using ocean-bottom DAS for passive observations of Scholte interface waves, we may estimate the S-wave velocity model of marine sediments through the inversion of their

dispersion curves computed from noise correlation virtual source gathers as shown in Cheng et al. (2021); Williams et al. (2021); Spica et al. (2022); Lior et al. (2022). The virtual source gathers from passive seismic data must be computed and used as the input to the velocity inversion from their dispersion analysis. Such computation could be time consuming, because we might need to stack several hours of data just to generate one stable dispersion curve.

When the surficial marine sediments have low S-wave velocities, seismo-acoustic resonances such as S-wave resonances are often observed (Godin et al., 2021). Then, we may use these phenomena to characterize the geophysical information of the sediments, instead of computing 1D velocity models from the Scholte interface waves observed in virtual source gathers.

According to Taweesintananon et al. (2023), S-wave resonances recorded by ocean-bottom fiber-optic DAS can be used to map the geologic structure of the corresponding LVL (soft marine sediments). In the next sections, we elaborate on the concept of S-wave resonances to determine not only the geologic structure but also the S-wave velocity model of the near-surface LVL in Svalbard, Norway. Here, we use S-wave resonance frequencies obtained from the DAS data for this purpose. Furthermore, we will show how the combined use of the S-wave resonance data from DAS and the P-wave seismic reflection data from near-surface geophysical site surveys can determine the thickness and S-wave velocity of the LVL. Svalbard is an Arctic archipelago at the northwestern edge of the Barents Shelf, far north of Norway. An overview of the geoscientific exploration in Svalbard is given by Dallmann (2015).

METHODS

Data acquisition

We used the standard single-mode G.652D fibers in two existing subsea fiber-optic telecommunication cables. The two cables were installed into the soft sediments at 0–2 m depth below the seafloor, between Longyearbyen and Ny-Ålesund in Svalbard, Norway (Figure 1). We denote the two cables as the inner and outer cables. Each cable is approximately 250 km long and contains 24 optical fibers. The cables are owned and operated by Sikt, which is the National Research and Education Network in Norway.

We connected an interrogator to each end of the cables. In total, four OptoDAS interrogators are used for DAS data recording: the ends of the inner and outer cables in Longyearbyen, and the other ends of the inner and outer cables in Ny-Ålesund. The OptoDAS interrogator is developed by Alcatel Submarine Networks. It sends linear optical frequency-modulated swept pulses into the optical fiber and receives the pulses backscattered from the inhomogeneities inside the fiber (Waagaard et al., 2021). It calculates the time-differentiated phase changes of consecutive backscattered pulses with spatial averaging corresponding to every spatially sampled position along the fiber. Then, these data are used to determine the longitudinal strains of the fiber at each sampling point.

In this experiment, we used light pulses with the free-space wavelength of 1550 nm and the sampling period of 1×10^{-8} s at the optical receiver. Defined by regions

of interest, we extract approximately 33,750 channels sampled every 4.08 m along the fiber from 0 to 135 km from each interrogator. Figure 1 shows a map of the two telecommunication cables used in our experiment. The DAS data were continuously recorded using 1.6 ms time sampling interval throughout the survey. The gauge length is 8.16 m. The backscattered signal strength decays by approximately 0.2 dB/km one-way along the cable, amounting to -40 dB over 100 km cable for the DAS measurement. The data were transferred in near-real-time to NTNU in Trondheim, Norway, over Sikt's telecommunication network for further analysis.

Data processing

In this study, we focus on the seismo-acoustic analysis of DAS data at frequencies below 20 Hz. Therefore, we resample the DAS strain data from 1.6 to 20 ms time sampling intervals with an antialiasing filter at 80% of the output Nyquist frequency of 25 Hz. Data resampling also reduces the computational cost for analyzing data over a long time window. After that, we attenuate interrogator noise that occurs in every DAS recording channel. First, we obtain the single-trace interrogator noise model by stacking (a mean calculation) all the DAS data traces in the first 40 km of the cable, in which the instrument noise level is low. Then, we subtract the noise model from every trace of the DAS data. The resampled data after the interrogator noise removal are used in our analysis.

S-wave resonances

Wave propagation modes caused by either P- or S-waves can occur in any solid layer below the seafloor. S-wave resonances are typically observed at frequencies between 0.3 and 7.5 Hz, when the surficial marine sediments over a rock substrate have low S-wave velocities (Godin et al., 2021). However, there are no upper nor lower limits to their frequencies. These resonances are generated by multiple normal reflections of S-waves. S-wave resonances as well as the normal modes and propagation modes of S-waves in the seafloor sediments are discussed and studied in several publications (Webb, 1998; Stephen et al., 2003). These phenomena are observable using ocean-bottom DAS as shown in Taweesintananon et al. (2023).

According to Williams et al. (2021) based on Hamilton (1976), unconsolidated marine sediments typically exhibit power-law S-wave velocity in the top tens of meters corresponding to the steep gradient in confining pressure below the seafloor. Based on the theoretical explanation given by Godin and Chapman (1999), we may investigate this phenomenon using a power-law S-wave velocity profile of the soft seafloor sediments with constant density in the simple power-law form:

$$c_s\left(z_s\right) = c_{s,0} z_s^{\nu}\,, \tag{1}$$

where z_s is the depth below the seafloor as a fluid-solid interface, $c_{s,0}$ represents the S-wave velocity at 1 m below the seafloor, and ν is the order of scaling (the exponent). Here, $c_{s,0}$ and ν are the non-negative constants, whereas z_s equals zero at the seafloor and is positive downward (toward the center of the Earth).

Let $z_s = H_s$ be a rigid boundary, so that the soft-sediment thickness is equal to H_s. According to Godin and Chapman (1999, equation 17), the nth S-wave resonance frequency can be determined from

$$f_{s,n} = \frac{c_{s,0}\,(1-\nu)\,j_{m,n}}{2\pi H_s^{1-\nu}}\,, \tag{2}$$

where n is a positive integer indicating the order of the normal mode, $m = \frac{2\nu-1}{2(1-\nu)}$ is a monotonically increasing function of ν varying between $-1/2$ and $+\infty$ for $0 \leq \nu \leq 1$, and $j_{m,n}$ is the nth positive zero of the Bessel function of the mth order $J_m(x)$. Note that m can be a fractional number, an integer, or a real number.

Equation 2 gives the exact formula for the nth S-wave resonance frequencies. However, this formula is not a form for practical uses. To simplify it, we can apply the asymptotic expansion for the Bessel function zeros when $n \gg 1 + m^2$, then we obtain (Godin and Chapman, 1999, equation 18)

$$f_{s,n} \approx \frac{\left(n + \frac{m}{2} - \frac{1}{4}\right) c_{s,0}\,(1-\nu)}{2H_s^{1-\nu}} + \mathcal{O}\left(\frac{1}{n}\right)\,. \tag{3}$$

Furthermore, using $m = \frac{2\nu-1}{2(1-\nu)}$, we rewrite equation 3 as

$$f_{s,n} \approx \frac{\left((2n-1)\,(1-\nu) + \frac{1}{2}\nu\right) c_{s,0}}{4H_s^{1-\nu}} + \mathcal{O}\left(\frac{1}{n}\right)\,. \tag{4}$$

Equation 4 approximately defines the nth S-wave resonance frequency corresponding to the S-wave velocity model in the power-law form in equation 1. In this form, we derive the average S-wave velocity over the sediment thickness H_s by

$$c_{s,\mathrm{avg}} = \frac{1}{H_s}\int_0^{H_s} c_s\,(z_s)\;dz_s = \frac{c_{s,0}H_s^{\nu}}{1+\nu}\,. \tag{5}$$

Note that, for a constant velocity model where $\nu = 0$, equation 4 is reduced to $f_{s,n} = (2n-1)\, c_{s,0}/\,(4H_s)$, which is the same formula as the normal mode frequency in the water column.

In this paper, we fundamentally use equation 4 for velocity estimation. We are aware that the equation is not exact, and it relies on the assumption that $n \gg 1+m^2$. Therefore, it could cause computational errors, when applied to the resonance frequencies of a small order such as $n = 1$. First, we analyze the first and the second S-wave resonance frequencies, i.e., $f_{s,1}$ and $f_{s,2}$. Then, we determine the S-wave velocity model defined by $c_{s,0}$ and ν based on equation 1. Given the S-wave resonance frequencies $f_{s,1}$ and $f_{s,2}$, we can determine the ν parameter from equation 4 (see Appendix A for the derivation):

$$\nu = \frac{6f_{s,1} - 2f_{s,2}}{5f_{s,1} - f_{s,2}}\,. \tag{6}$$

On the other hand, we can determine $c_{s,0}$ by rearranging equation 4 as

$$c_{s,0} = \frac{4H_s^{1-\nu} f_{s,n}}{(2n-1)\,(1-\nu) + \frac{1}{2}\nu}\,. \tag{7}$$

Therefore, given the sediment thickness H_s and the first S-wave resonance frequency $f_{s,1}$, we rewrite equation 7 to $c_{s,0} = 4H_s^{1-\nu} f_{s,1}/\left(1 - \frac{1}{2}\nu\right)$. Thus, we can determine the S-wave velocity model of the sediment through equations 1, 6 and 7.

Note that, to determine the S-wave velocity model through equations 1, 6 and 7, the sediment thickness H_s and the S-wave resonance frequencies $f_{s,1}$ and $f_{s,2}$ must be given. The sediment thickness could be estimated from the existing active seismic reflection data in the survey area. Nevertheless, these data are normally unavailable

in frontier areas. If active seismic reflection data are unavailable, we must estimate the sediment thickness H_s from the DAS strain data. In this case, we may determine the sediment thickness from the average S-wave velocity of the sediment. From equations 4 and 5, we can derive

$$H_s = \frac{\left((2n-1)\left(1-\nu^2\right)+\frac{1}{2}\nu\left(1+\nu\right)\right)c_{s,\mathrm{avg}}}{4f_{s,n}}\,. \tag{8}$$

Therefore, the sediment thickness H_s can be estimated from the average S-wave velocity $c_{s,\mathrm{avg}}$ and the first S-wave resonance frequency $f_{s,1}$ using equation 8.

In this paper, we demonstrate two cases of using S-wave resonances for near-surface characterization. In case 1, we use only the ocean-bottom DAS strain data to determine the S-wave velocity model of the near-surface LVL. Here, we estimate the LVL thickness using equation 8 and, then, determine the S-wave velocity model through equations 1, 6 and 7. In case 2, we use both of the DAS data and the existing active seismic reflection data over the same recording positions. Here, we derive the LVL thickness by interpreting the associated P-wave reflections in the existing seismic data. Then, we determine the S-wave velocity model of the sediment through equations 1, 6 and 7.

RESULTS AND DISCUSSION

Analysis of S-wave resonance frequencies

Ocean-bottom DAS can measure S-wave resonances corresponding to the predominantly horizontal particle motion parallel to the fiber axis associated with the S-wave

propagation in the near-surface LVL as discussed by Taweesintananon et al. (2023). The external seismic energy from earthquakes can enhance the S-wave resonances at the higher orders. In this paper, we analyze the first and the second resonance frequencies from such events recorded by ocean-bottom DAS.

Figure 2 shows the ocean-bottom DAS strain data along the inner cable after band-pass filtering between 0.01 and 20 Hz. Figure 2a shows the typical strain data in the 1200 s time window from 2022-08-22T12:00:07Z that contain no strong seismic waves from earthquakes. In this time window, we observe linear dipping wavetrains in all the recording channels. These wavetrains are referred to as the responses from the ocean-bottom loading pressure variations associated with the overlying OSGWs (Taweesintananon et al., 2023). On the other hand, Figure 2b shows the strain data in the 1200 s time window from 2022-08-19T09:15:25Z that contain seismic waves from a local earthquake with epicenter at a few hundred kilometers south of the southern coastline of the Svalbard archipelago. Here, P- and S-waves arrive at approximately 280 s as marked in Figure 2b.

In this paper, we estimate the power spectral density, also called the power spectrum, of a DAS data trace by using the standard periodogram method, which is the square of its discrete Fourier transform or the discrete Fourier transform of its autocorrelation function (Sheriff, 2002). Here, the normalization factor is one (unscaled) for the forward Fourier transform. We continuously monitored the DAS data and found that the first S-wave resonance is consistently presented in the power spectra throughout the recording. The resonance is amplified by not only earthquakes but

also strong wind and severe weather, which typically cause the stronger ambient noise in the ocean-bottom DAS data. The power spectra computed from the DAS strain data in Figure 2a and 2b are illustrated in the frequency-distance (f-x) domain in Figure 3a and 3b, respectively. In Figure 3b, we find that the amplitudes of S-wave resonances at multiple orders are enriched by the seismic waves from earthquakes. Our result agrees with the observation made in Taweesintananon et al. (2023, Figures 5b and 8b), which compare the f-x power spectra from the 1200 s time segments before and after the P-wave seismic arrival from an earthquake.

Because of the strong input energy from seismic waves, the first and the second S-wave resonances are clearly observed in the f-x power spectra shown in Figure 3b. We manually pick the first and the second S-wave resonance frequencies ($f_{s,1}$ and $f_{s,2}$) along the inner cable from the power spectra in Figure 3b. According to equation 6, the frequency picking is done with the constraint that $f_{s,2} \leq 3f_{s,1}$ for $0 \leq \nu \leq 1$. The frequency picks are plotted on both the f-x power spectra (Figure 3a and 3b) together with the maximum frequency of OSGWs and the cutoff frequencies for the guided P-waves in the water layer, which are estimated by equations 6 and 11 in Taweesintananon et al. (2023).

In addition, Figure 4 shows enlarged displays of the f-x power spectra with and without earthquakes along the outer cable near Ny-Ålesund. In Figure 4a, we observe only the first-order S-wave resonance in the ambient noise spectra, and it is difficult to interpret the S-wave resonances at the higher orders. In the presence of strong seismic waves from the earthquake, the S-wave resonances at multiple orders become

much more prominent as shown in Figure 4b. Then, we can easily pick the first and the second S-wave resonance frequencies ($f_{s,1}$ and $f_{s,2}$) as plotted in Figure 4b.

The interpretation of S-wave resonance frequencies is crucial for characterizing the near-surface LVL. As suggested by equation 6, the S-wave resonance frequencies of at least two different orders are used to determine the velocity variation versus depth. Hence, we emphasize that strong seismic energy from sufficiently large earthquakes is required to trigger the modes at the higher orders of the S-wave resonances and enable us to analyze the resonance frequencies at multiple orders. To achieve even clearer f-x power spectra for picking the resonance frequencies more precisely, we may stack the spectra from several earthquakes. In this paper, we have not investigated how to optimally stack such spectra. However, we believe that the stacking quality depends on the consistency of the DAS responses to those earthquakes with different epicentral distances, azimuth directions, sizes, etc.

In this paper, we have not analyzed the S-wave resonance amplitude characteristics in the power spectrum in detail. However, we observe that the resonance amplitude varies with the position along the cable as shown in Figure 4a and 4b. Therefore, the topography of the LVL, i.e., the lateral variation of the sediment thickness, probably affects the S-wave resonance amplitude. We speculate that the amplitude could be strong and focused when there is no lateral change in the LVL thickness. In contrast, the amplitude could be weak and dispersed when there is strong lateral variation of the LVL thickness. The impact of the topography on the S-wave resonance amplitude observed by ocean-bottom fiber-optic DAS is not in the scope of this paper but could

be an interesting topic for further study.

In addition, it is beyond the scope of this paper to study the generation mechanism of the S-wave resonances. In Figures 3 and 4, we clearly observe that the S-wave resonances are amplified by the arrivals of the body waves, i.e., the P- and S-waves generated from an earthquake. However, we know from previous publications such as Williams et al. (2021) that DAS in subsea fiber-optic cables also detect Scholte interface waves with the frequency range between 0.3 and 5 Hz propagating along the seafloor. Therefore, we believe that the S-wave resonances observed in this paper are attributed to a combination of Scholte interface waves at the seafloor from ambient noise and the body waves from earthquakes. Note that the Scholte interface waves are not directly observable in the ambient noise data unless they are generated from a strong source. However, they can be observed from noise correlation virtual source gathers using interferometry techniques as described by Williams et al. (2021). We might be able to learn more about the generation mechanism of the S-wave resonances by comparing in detail (for instance, using synthetic modeling) how their amplification levels vary with the Scholte interface waves and seismic body waves.

In the two following subsections, we use the first and the second S-wave resonance frequencies along the inner cable discussed previously to build S-wave velocity models of the subsurface LVL. We demonstrate this near-surface characterization in two cases: case 1 for using S-wave resonance data only, and case 2 for using both S-wave resonance and P-wave seismic reflection data.

Case 1: Near-surface characterization using S-wave resonance

In case 1, we use only the ocean-bottom DAS strain data for LVL thickness estimation and its S-wave velocity model building. Here, we will analyze the ocean-bottom DAS strain data and build the S-wave velocity model as defined by equation 1. Using equation 6, we can determine the ν parameter from the first and the second S-wave resonance frequencies ($f_{s,1}$ and $f_{s,2}$) resulting from the analysis described in the previous subsection. Next, we determine the $c_{s,0}$ parameter using equation 7. The inputs to this calculation include the ν parameter, the first S-wave resonance frequency $f_{s,1}$, and the sediment thickness H_s. However, the sediment thickness H_s is unknown if only the S-wave resonance data are available for our analysis. When this is the case, we must assume that we know the average S-wave velocity in order to determine the sediment thickness H_s using equation 8.

According to Albaric et al. (2021, Figures 2b and 8b), in the Adventdalen area near Longyearbyen in Svalbard, the S-wave velocity of the near-surface sediments is found to be approximately 200 m/s in the upper 50 m, increasing to approximately 450 m/s at 75 m depth, below which the velocity sharply rises to approximately 1800 m/s within 20 m vertical distance. Based on these results, we assume that the average S-wave velocity $c_{s,\text{avg}}$ in the Isfjorden area is approximately 200 m/s. Thus, we can determine the sediment thickness H_s by inserting $c_{s,\text{avg}} = 200$ m/s, the ν parameter resulting from equation 6, and the first S-wave resonance frequency $f_{s,1}$ into equation 8. Then, we compute the $c_{s,0}$ parameter using equation 7. Finally, the computed $c_{s,0}$ and ν parameters constitute the power-law S-wave velocity model in

equation 1.

Figure 3c shows the S-wave velocity model and the corresponding depth profile of the LVL along the first 130 km distance of the inner cable as computed in case 1. This S-wave velocity model is derived from the computation using the interpreted S-wave resonance frequencies and the average S-wave velocity $c_{s,\mathrm{avg}} = 200$ m/s. The model represents the near-surface LVL along the inner cable in the Isfjorden area. According to Forwick and Vorren (2010), this LVL should be referred to as the shallow glacimarine sediments that rest upon the bedrock, namely, the acoustic basement, in the Isfjorden area. Hence, the base of the LVL model represents the top of the bedrock defined in Forwick and Vorren (2010).

Furthermore, we can compute the S-wave velocity model between Longyearbyen and Ny-Ålesund along the entire 250 km distance of the outer cable. Here, we separately analyze the ocean-bottom DAS strain data recorded from the outer cable concurrently by one interrogator in Longyearbyen and the other interrogator of the same model in Ny-Ålesund. The frequency analysis is conducted over the 1200 s time windows that contain the seismic energy from the same earthquake as presented in Figure 2b. Figure 5 shows the result from the interrogator in Ny-Ålesund, and Figure 6 shows the result from the interrogator in Longyearbyen. The S-wave velocity model of the LVL estimated from these two interrogators gives a rough picture of the near-surface geologic structure across the ocean between Longyearbyen and Ny-Ålesund.

Equation 2 implies that S-wave resonance frequencies are independent of the wa-

ter depth. Accordingly, the LVL thickness estimated from S-wave resonances can be uncorrelated with the water depth. In Figure 5, we see that the LVL thickness estimated in case 1 is not correlated with water depth approximately at the cable distance 200 km. Here, there is a sudden change in the first S-wave resonance frequency approximately at the cable distance 200 km, while the seafloor is gradually dipping down from the cable distances 195 to 210 km. This observation confirms the independence between the water depth and the results from our proposed S-wave resonance method.

With an assumption of the average S-wave velocity of the LVL in the Isfjorden area, we can build the associated depth-variant S-wave velocity model from ocean-bottom DAS strain data as shown in case 1. Thus, we can model the depth-variant S-wave velocity of the LVL if there is sufficient seismic energy in the DAS data recording for analyzing the first and second S-wave resonance frequencies. Moreover, by using four interrogators as mentioned in the Methods section, it is possible to build such an S-wave velocity model between Longyearbyen and Ny-Ålesund along both inner and outer cables. The accuracy of the model depends on the accuracy of the average S-wave velocity that we assumed for the computation. To improve the accuracy of the S-wave velocity model of the LVL, we must know the LVL thickness, which could be obtained from another geophysical survey.

Case 2: Near-surface characterization using S-wave resonance and P-wave seismic reflection data

In case 2, we will improve the accuracy of the S-wave velocity model of the LVL by incorporating an existing P-wave seismic reflection data set into our analysis. In this case, we use the 2D marine P-wave seismic reflection data that are published by Forwick and Vorren (2010) in order to determine the LVL thickness for S-wave velocity model building.

Figure 7 shows a survey map of the 2D sparker profile "Line-03-050BS" (Forwick and Vorren, 2010, Figure 2). This 2D marine P-wave seismic reflection data set was acquired in 2003 with R/V Jan Mayen using a 700 J Bennex multielectrode sparker as the seismic source. We use this sparker profile as the reference, because it is partially overlapped with the inner cable used for DAS data recording in our experiment as shown in Figure 7.

Note that, in case 2, the LVL thickness is interpreted from the 2D seismic data shown in Figure 8a. In this figure, we interpret two seismic traveltime horizons, i.e., the seafloor and the base of the LVL, based on Forwick and Vorren (2010). The image portions in the two rectangular regions in Figure 8a are enlarged in Figure 9a and 9b. Note that Figure 9a is comparable to Figure 7A in Forwick and Vorren (2010). Furthermore, we assume that the average P-wave velocity in water is approximately 1490 m/s, and the average P-wave velocity in the LVL is approximately 1600 m/s (Forwick and Vorren, 2010, page 165). Hence, we can compute the thickness of the

water column and the LVL from the two interpreted traveltime horizons. That is, we obtain the sediment thickness H_s from the 2D P-wave seismic reflection data.

In contrast, the S-wave resonance frequencies are interpreted from the DAS strain data shown in Figure 3b. Therefore, we first project the interpreted S-wave resonance frequencies onto the 2D seismic line perpendicularly. Then, we obtain the first and the second S-wave resonance frequencies ($f_{s,1}$ and $f_{s,2}$) along the 2D seismic line "Line-03-050BS."

In case 2, we estimate the S-wave velocity model along the 2D seismic line "Line-03-050BS" by following the process described in the Methods section. First, we use equation 6 to compute the ν parameter from the S-wave resonance frequencies. Then, we use equation 7 to compute the $c_{s,0}$ parameter from the sediment thickness H_s, the first S-wave resonance frequency $f_{s,1}$, and the ν parameter. Finally, the computed $c_{s,0}$ and ν parameters constitute the power-law S-wave velocity model in equation 1. Thus, we obtain the S-wave velocity model along the 2D seismic line "Line-03-050BS."

In Figure 8, we compare the results of S-wave velocity model building in cases 1 and 2. All the results are spatially projected onto the 2D seismic line "Line-03-050BS," for which the data are shown in Figure 8a. Here, Figure 8b and 8c show the estimated S-wave velocity models of the LVL along the 2D seismic line resulting from cases 1 and 2, respectively.

In comparison with the 2D seismic data in Figure 8a, we observe that the structural depth and the S-wave velocity model of the LVL derived from case 2 (Figure 8c) are different from those that are derived from case 1 (Figure 8b). The structural depth

of the LVL base in case 2 is more accurate, because it relies on the corresponding seismic horizon interpreted from the 2D seismic reflection data shown in Figure 8a. Therefore, we may infer that the S-wave velocity model in case 2 is more accurate than the model derived from case 1.

Moreover, we see that the estimated S-wave velocity in case 2 varies laterally within the LVL formation as shown in Figure 8c. Specifically, we observe high S-wave velocity on the wedge of the LVL base around FFID 12000 and on the synclines of the LVL base around FFID 6500, 5000, and 3500. However, such high S-wave velocity deposits do not exist at the syncline around FFID 9000. Therefore, we believe that the variation of the S-wave velocity result from spatial variation of the sedimentary deposition.

Here, we find that the sediments or deposits with high S-wave velocity in the LVL are connected to the accumulation of basal tills (unit S1) and the sedimentary wedges (unit S3) exclusively found on the slopes facing toward the fjord mouths to the West, which is the direction of palaeo-ice flow (Forwick and Vorren, 2010, Figures 6B and 7). Moreover, we note that the sediments belonging to units S1–S3 typically have higher densities and higher P-wave velocities than the overlying deposits. Accordingly, the S-wave velocities of the sediments in units S1–S3 tend to be higher than those in the other shallower units. In addition, the basal tills are the lowest unit of the LVL, and they generally appear as a thin deposit unit of less than 10 m thickness resting directly upon the bedrock or the acoustic basement throughout the entire fjord system (Forwick and Vorren, 2010, page 165). According to Forwick and Vorren (2010, page

168), their thickness could be a maximum of 55 m in the Svensksunddjupet area, which is approximately at FFID 13000 in Figure 8.

Based on the result from case 2 shown in Figure 8c, the deposits with the S-wave velocity ranging between 300 and 450 m/s probably indicate the sedimentary wedges (unit S3), whereas the deposits with the S-wave velocity higher than 450 m/s probably indicate the accumulation of basal tills (unit S1). It is also possible that the areas with high S-wave velocities could be referred to as the thicker sequences or thicker accumulations of basal tills. As marked in Figure 8c, we interpret that unit S3 deposits are present in the areas where the S-wave velocity is higher than 300 m/s. These interpreted locations of the unit S3 deposits are well correlated with the distribution of the sedimentary wedges (unit S3) reported by Forwick and Vorren (2010, Figure 6B), which is also illustrated on the map in Figure 7. Thus, it is possible to use the S-wave velocity model of the LVL estimated from case 2 to map the distribution of glacigenic sediments and landforms deposited as units S1–S3 along the 2D seismic line.

CONCLUSION

In this paper, we use the interpreted S-wave resonance frequencies from ocean-bottom fiber-optic DAS data to derive the S-wave velocity model of the near-surface marine sediments, i.e., the LVL beneath the seafloor. To derive the S-wave velocity model, we must solve for both the sediment thickness and the S-wave velocity, which are the two parameters that control the two-way traveltime of the wave with normal

reflection, i.e., $t = 2H_s/c_s$. When the traveltime information is extracted from the recorded seismic data, we can determine the exact solution of one parameter only if we know the exact value of the other parameter.

We compare the estimation of the LVL thickness and S-wave velocity using only S-wave resonance data (case 1) and the estimation using both S-wave resonance data and P-wave seismic reflection data (case 2). Case 1 assumes a constant value of the average S-wave velocity parameter. On the other hand, case 2 assumes that we know the sediment thickness parameter from interpretation of the P-wave seismic reflection data. The results from these two methods suggest a potential application of S-wave resonances to the characterization of the corresponding LVL. The estimated S-wave velocities of the near-surface LVL in Svalbard ranges between 100 and 600 m/s. The method using only S-wave resonances shown in case 1 could have errors in estimating the layer thickness and S-wave velocity, especially in areas with strong lateral variation of the S-wave velocity. Such errors can be eliminated by supplying the layer thickness information from other methods. Hence, we recommend estimating the S-wave velocity model of the LVL using S-wave resonance data together with the layer thickness determined from, for example, P-wave seismic reflection data as shown in case 2. The use of the interpreted sediment thickness from P-wave reflection data reduces the uncertainty and improves the accuracy in S-wave velocity model building from S-wave resonance frequencies.

ACKNOWLEDGMENTS

The authors acknowledge the Research Council of Norway (RCN) and the sponsors of the Geophysics and Applied Mathematics in Exploration and Safe production Project (GAMES; RCN grant no. 294404), and the Centre for Geophysical Forecasting (CGF; RCN grant no. 309960) at NTNU for financial support. The authors thank Sikt for providing access to their fiber-optic cables between Longyearbyen and Ny-Ålesund and operating the data transfer through their network between Svalbard and Trondheim. The authors thank NORSAR for providing one interrogator for the outer cable in Longyearbyen.

AUTHOR CONTRIBUTIONS

M. Landrø conceived and designed the experiment. R. A. Rørstadbotnen and M. Forwick collected data. K. Taweesintananon and R. A. Rørstadbotnen processed the data and prepared the visualizations. K. Taweesintananon, R. A. Rørstadbotnen, and M. Landrø analyzed the data with support from S. E. Johansen, B. Arntsen, M. Forwick, and A. Hanssen. M. Landrø validated the research outputs, acquired the funding, and managed the project. K. Taweesintananon wrote the original draft of the manuscript. All the authors conducted the review and editing of the manuscript.

COMPETING INTERESTS

Author K. Taweesintananon is employed by PTT Exploration and Production Public Company Limited. The remaining authors declare that the research was conducted in the absence of any commercial or financial relationships that could be construed as a potential conflict of interest.

DATA AND MATERIALS AVAILABILITY

Data associated with this research are available and can be accessed via the following URL: `https://doi.org/10.18710/ONGBEV`.

APPENDIX A

DERIVATION OF EQUATION 6

Using equation 4, we derive the first and second S-wave resonance frequencies as

$$f_{s,1} \approx \frac{\left(1 - \frac{1}{2}\nu\right) c_{s,0}}{4H_s^{1-\nu}}\,, \tag{A-1}$$

and

$$f_{s,2} \approx \frac{\left(3 - \frac{5}{2}\nu\right) c_{s,0}}{4H_s^{1-\nu}}\,. \tag{A-2}$$

Accordingly, we can estimate the ratio between the second and the first S-wave resonance frequencies as

$$\frac{f_{s,2}}{f_{s,1}} = \frac{3 - \frac{5}{2}\nu}{1 - \frac{1}{2}\nu}\,. \tag{A-3}$$

To determine the ν parameter, we rearrange equation A-3 and derive equation 6, i.e.,

$$\nu = \frac{6f_{s,1} - 2f_{s,2}}{5f_{s,1} - f_{s,2}}\,. \tag{A-4}$$

REFERENCES

Albaric, J., D. Kühn, M. Ohrnberger, N. Langet, D. Harris, U. Polom, I. Lecomte, and G. Hillers, 2021, Seismic monitoring of permafrost in Svalbard, Arctic Norway: Seismological Research Letters, **92**, 2891–2904.

Cheng, F., B. Chi, N. J. Lindsey, T. C. Dawe, and J. Ajo-Franklin, 2021, Utilizing distributed acoustic sensing and ocean bottom fiber optic cables for submarine structural characterization: Scientific Reports, 14.

Dallmann, W. K., ed., 2015, Geoscience Atlas of Svalbard: Norsk Polarinstitutt. Report, No. 148.

Dong, H., T.-D. Nguyen, and K. Duffaut, 2013, Estimation of seabed shear-wave velocity profiles using shear-wave source data: The Journal of the Acoustical Society of America, **134**, 176–184.

Dong, Y., S. Piao, L. Gong, G. Zheng, K. Iqbal, S. Zhang, and X. Wang, 2021, Scholte wave dispersion modeling and subsequent application in seabed shear-wave velocity profile inversion: Journal of Marine Science and Engineering, **9**.

Draganov, D., X. Campman, J. Thorbecke, A. Verdel, and K. Wapenaar, 2009, Reflection images from ambient seismic noise: GEOPHYSICS, **74**, A63–A67.

Forwick, M., and T. O. Vorren, 2010, Stratigraphy and deglaciation of the Isfjorden area, Spitsbergen: Norwegian Journal of Geology, **90**, 163–179.

Foti, S., F. Hollender, F. Garofalo, D. Albarello, M. Asten, P.-Y. Bard, C. Comina, C. Cornou, B. Cox, G. Di Giulio, T. Forbriger, K. Hayashi, E. Lunedei, A. Martin, D. Mercerat, M. Ohrnberger, V. Poggi, F. Renalier, D. Sicilia, and V. Socco,

2018, Guidelines for the good practice of surface wave analysis: a product of the InterPACIFIC project: Bulletin of Earthquake Engineering, **16**, 2367–2420.

Godin, O. A., and D. M. F. Chapman, 1999, Shear-speed gradients and ocean seismo-acoustic noise resonances: The Journal of the Acoustical Society of America, **106**, 2367–2382.

Godin, O. A., T. J. Deal, and H. Dong, 2021, Physics-based characterization of soft marine sediments using vector sensors: The Journal of the Acoustical Society of America, **149**, 49–61.

Hamilton, E. L., 1976, Shear-wave velocity versus depth in marine sediments: A review: GEOPHYSICS, **41**, 985–996.

Hartog, A. H., 2017, An introduction to distributed optical fibre sensors, 1 ed.: CRC Press.

He, H., L. Jiang, Y. Pan, A. Yi, X. Zou, W. Pan, A. E. Willner, X. Fan, Z. He, and L. Yan, 2023, Integrated sensing and communication in an optical fibre: Light: Science & Applications, **12**, 25.

Landrø, M., L. Bouffaut, H. J. Kriesell, J. R. Potter, R. A. Rørstadbotnen, K. Taweesintananon, S. E. Johansen, J. K. Brenne, A. Haukanes, O. Schjelderup, and F. Storvik, 2022, Sensing whales, storms, ships and earthquakes using an Arctic fibre optic cable: Scientific Reports, **12**, 19226.

Lindsey, N. J., T. C. Dawe, and J. B. Ajo-Franklin, 2019, Illuminating seafloor faults and ocean dynamics with dark fiber distributed acoustic sensing: Science, **366**, 1103–1107.

Lior, I., E. D. Mercerat, D. Rivet, A. Sladen, and J. Ampuero, 2022, Imaging an

underwater basin and its resonance modes using optical fiber distributed acoustic sensing: Seismological Research Letters, **93**, 1573–1584.

Sheriff, R. E., 2002, Encyclopedic dictionary of applied geophysics, 4th ed.: Society of Exploration Geophysicists, volume **13** *of* Geophysical References Series.

Sladen, A., D. Rivet, J. P. Ampuero, L. De Barros, Y. Hello, G. Calbris, and P. Lamare, 2019, Distributed sensing of earthquakes and ocean-solid Earth interactions on seafloor telecom cables: Nature Communications, **10**, 5777.

Spica, Z. J., J. C. Castellanos, L. Viens, K. Nishida, T. Akuhara, M. Shinohara, and T. Yamada, 2022, Subsurface imaging with ocean-bottom distributed acoustic sensing and water phases reverberations: Geophysical Research Letters, **49**, e2021GL095287.

Stephen, R. A., F. N. Spiess, J. A. Collins, J. A. Hildebrand, J. A. Orcutt, K. R. Peal, F. L. Vernon, and F. B. Wooding, 2003, Ocean seismic network pilot experiment: Geochemistry, Geophysics, Geosystems, **4**, 1092.

Taweesintananon, K., M. Landrø, J. R. Potter, S. E. Johansen, R. A. Rørstadbotnen, L. Bouffaut, H. J. Kriesell, J. K. Brenne, A. Haukanes, O. Schjelderup, and F. Storvik, 2023, Distributed acoustic sensing of ocean-bottom seismo-acoustics and distant storms: A case study from Svalbard, Norway: GEOPHYSICS, **88**, B135–B150.

Waagaard, O. H., E. Rønnekleiv, A. Haukanes, F. Stabo-Eeg, D. Thingbø, S. Forbord, S. E. Aasen, and J. K. Brenne, 2021, Real-time low noise distributed acoustic sensing in 171 km low loss fiber: OSA Continuum, **4**, 688–701.

Webb, S. C., 1998, Broadband seismology and noise under the ocean: Reviews of

Geophysics, **36**, 105–142.

Williams, E. F., M. R. Fernández-Ruiz, R. Magalhaes, R. Vanthillo, Z. Zhan, M. González-Herráez, and H. F. Martins, 2019, Distributed sensing of microseisms and teleseisms with submarine dark fibers: Nature Communications, **10**, 5778.

———, 2021, Scholte wave inversion and passive source imaging with ocean-bottom DAS: The Leading Edge, **40**, 576–583.

LIST OF FIGURES

200 to 250 km distance along the outer cable near Ny-Ålesund. (a) The f-x power spectra of the strain data without strong earthquakes in the 1200 s time window from 2022-08-19T08:55:29Z. (b) The f-x power spectra of the strain data with strong earthquakes in the 1200 s time window from 2022-08-19T09:15:29Z. (c) The structural depth profile below the sea level of the seafloor and the estimated LVL base, overlaid with the estimated S-wave velocity model of the LVL.

5 Frequency analysis of the DAS strain data with strong earthquakes recorded at 120 to 250 km distance of the outer cable by the interrogator in Ny-Ålesund. (a) The strain data in the 1200 s time window from 2022-08-19T09:15:29Z. (b) The f-x power spectra of the strain data in the 1200 s time window. (c) The structural depth profile below the sea level of the seafloor and the estimated LVL base, overlaid with the estimated S-wave velocity model of the LVL.

6 Frequency analysis of the DAS strain data with strong earthquakes recorded at 0 to 130 km distance of the outer cable by the interrogator in Longyearbyen. (a) The strain data in the 1200 s time window from 2022-08-19T09:15:27Z. (b) The f-x power spectra of the strain data in the 1200 s time window. (c) The structural depth profile below the sea level of the seafloor and the estimated LVL base, overlaid with the estimated S-wave velocity model of the LVL.

7 Enlarged map of the DAS arrays and the reference seismic data along the Isfjorden. The 2D seismic data "Line-03-050BS" is plotted and annotated with field file identifiers (FFIDs), namely, the shot numbers. The distribution of the sedimentary wedges (unit S3) reported in Figure 6B of Forwick and Vorren (2010) is also shown here. The map is referencing the projected coordinate system in Universal Transverse

Mercator (UTM) Zone 33 North on WGS 84 (World Geodetic System 1984) geodetic coordinate reference system.

8 S-wave velocity models of the LVL. (a) The 2D seismic reflection data "Line-03-050BS" in the time domain overlaid with the interpreted seismic horizons of the seafloor and LVL base. The black dotted rectangles indicate the enlarged seismic sections shown in other figures. (b) The S-wave velocity model estimated in case 1 using only the DAS data (no other seismic data are involved). (c) The S-wave velocity model estimated in case 2, in which the LVL thickness is derived from the interpretation of the existing 2D seismic data shown in (a). The sedimentary wedges (unit S3) in the LVL are marked in (c) in correlation with their geographical distribution shown in Figure 7.

9 Enlarged 2D seismic sections in the rectangular regions shown in Figure 8a. (a) The section in Svensksunddjupet area. (b) The section in Norseliusdjupet area. A toponymic map presenting the key geographical locations in the Isfjorden area is shown in Figure 7.

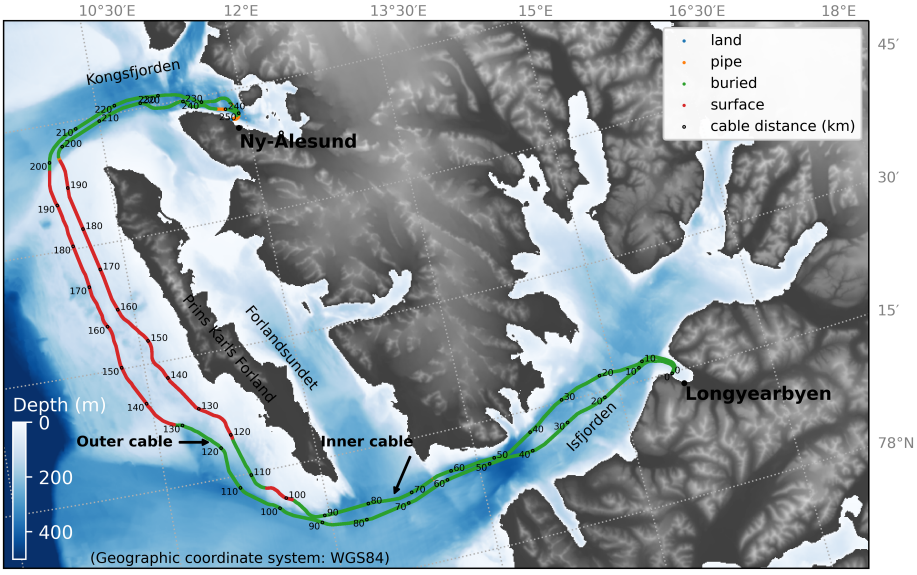

Figure 1: Map of the two subsea fiber-optic telecommunication cables for DAS recording. The inner and outer cables start from Longyearbyen, go along the Isfjorden toward the ocean to the West, bypass Prins Karls Forland to the North, enter the Kongsfjorden, and end in Ny-Ålesund. The cables are annotated with the distance in km from the shore in Longyearbyen and colored with their surficial conditions.

– **GEO-2023-0530.R2.accepted**

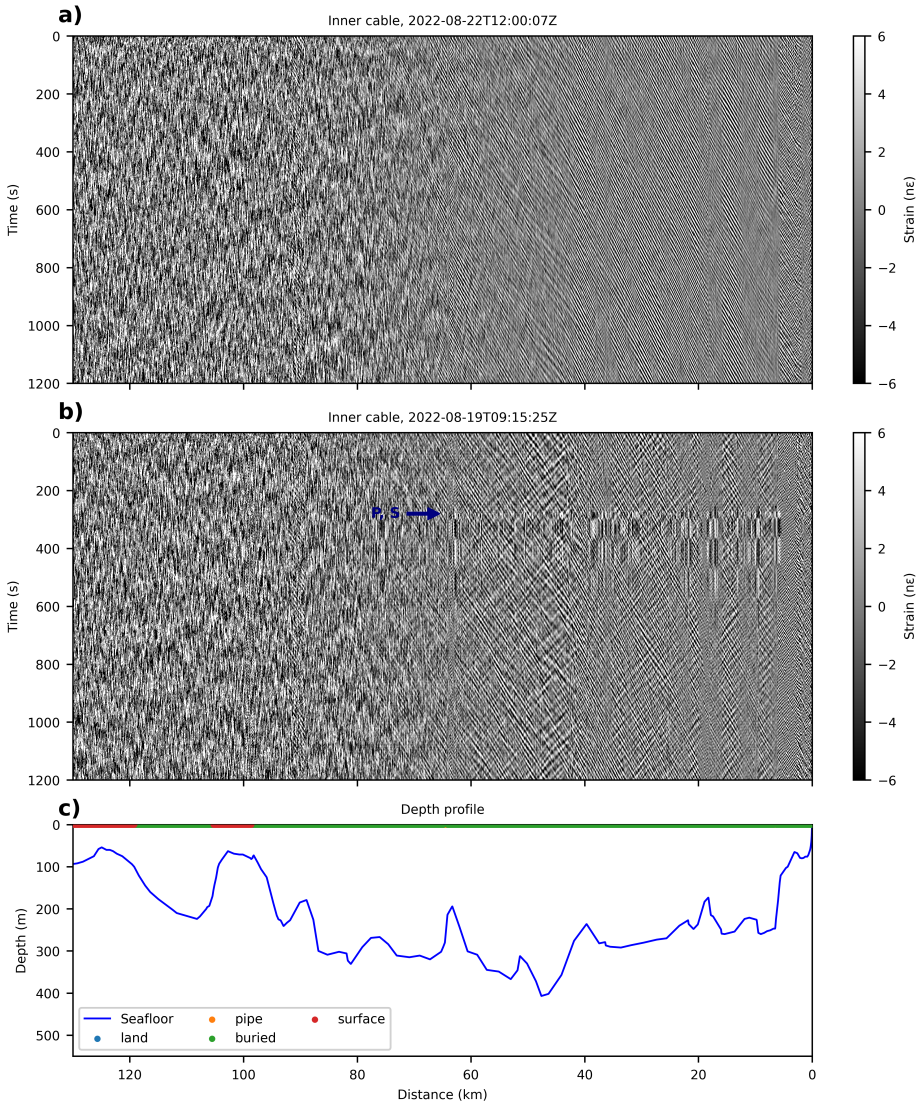

Figure 2: Ocean-bottom DAS strain data with and without earthquakes recorded at 0 to 130 km distance from Longyearbyen's shore along the inner cable. (a) The strain data without strong earthquakes in the 1200 s time window from 2022-08-22T12:00:07Z. (b) The strain data in the 1200 s time window from 2022-08-19T09:15:25Z containing strong seismic waves from a local earthquake in Svalbard. (c) The structural depth profile below the sea level of the seafloor, in which the surficial conditions of the DAS receivers along the inner cable are marked at the top of the plotting area.

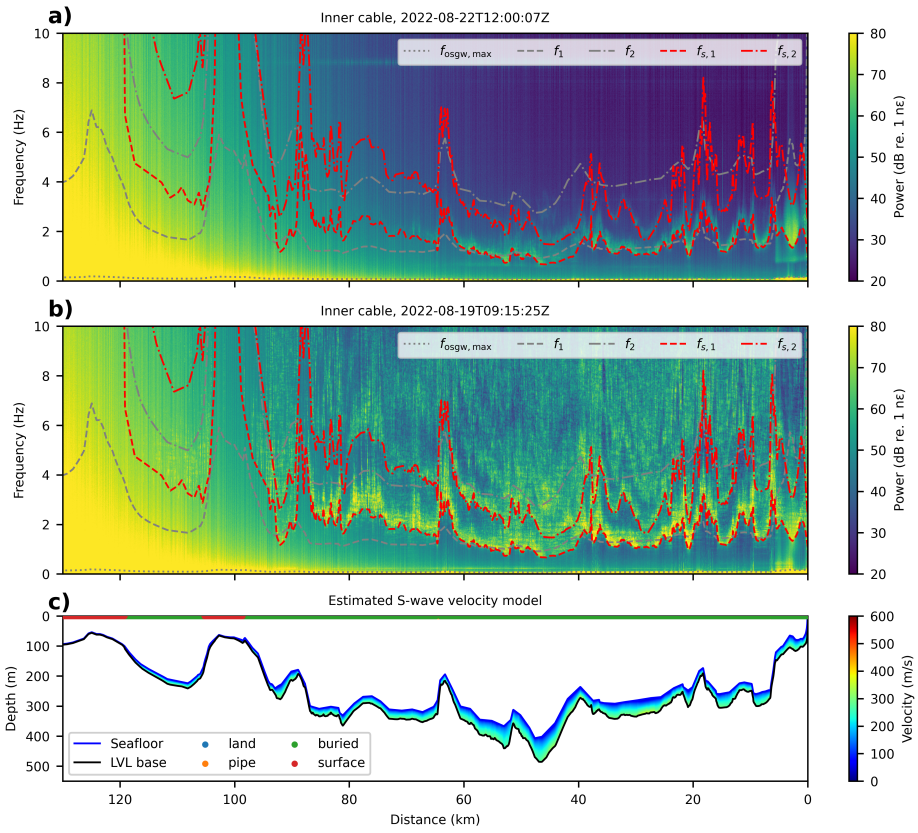

Figure 3: Frequency analysis of the DAS strain data at 0 to 130 km distance along the inner cable presented in Figure 2. (a) The f-x power spectra of the strain data without strong earthquakes in the 1200 s time window from 2022-08-22T12:00:07Z shown in Figure 2a. (b) The f-x power spectra of the strain data with strong earthquakes in the 1200 s time window from 2022-08-19T09:15:25Z shown in Figure 2b. (c) The structural depth profile below the sea level of the seafloor and the estimated LVL base, overlaid with the estimated S-wave velocity model of the LVL.

– **GEO-2023-0530.R2.accepted**

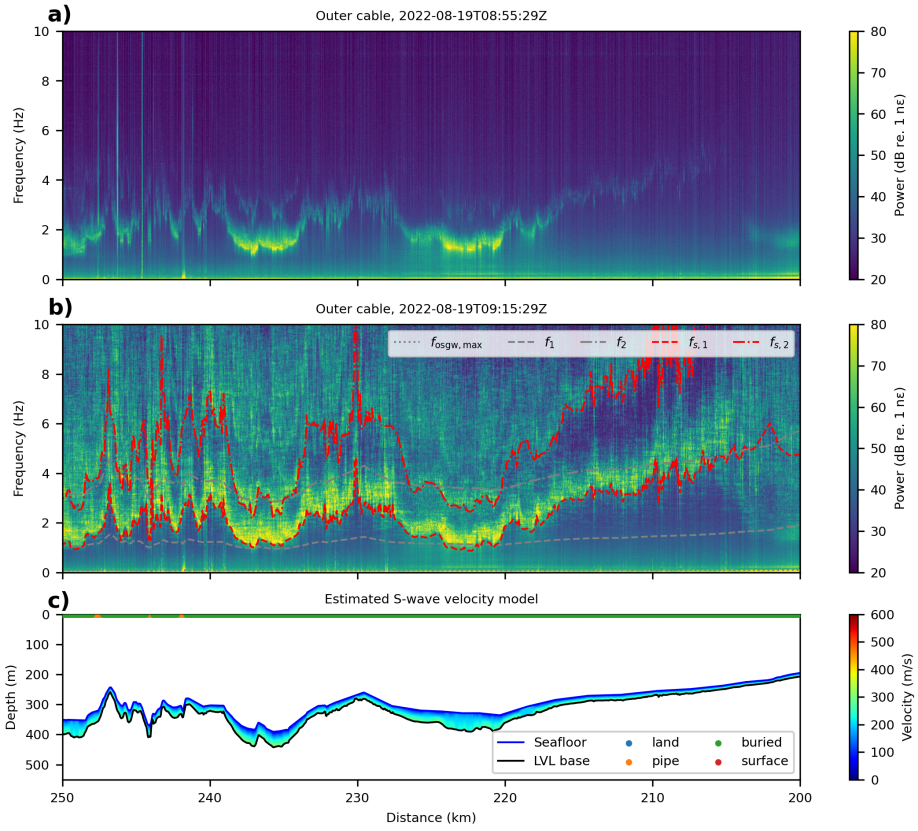

Figure 4: Frequency analysis of the DAS strain data with and without earthquakes at 200 to 250 km distance along the outer cable near Ny-Ålesund. (a) The f-x power spectra of the strain data without strong earthquakes in the 1200 s time window from 2022-08-19T08:55:29Z. (b) The f-x power spectra of the strain data with strong earthquakes in the 1200 s time window from 2022-08-19T09:15:29Z. (c) The structural depth profile below the sea level of the seafloor and the estimated LVL base, overlaid with the estimated S-wave velocity model of the LVL.

– **GEO-2023-0530.R2.accepted**

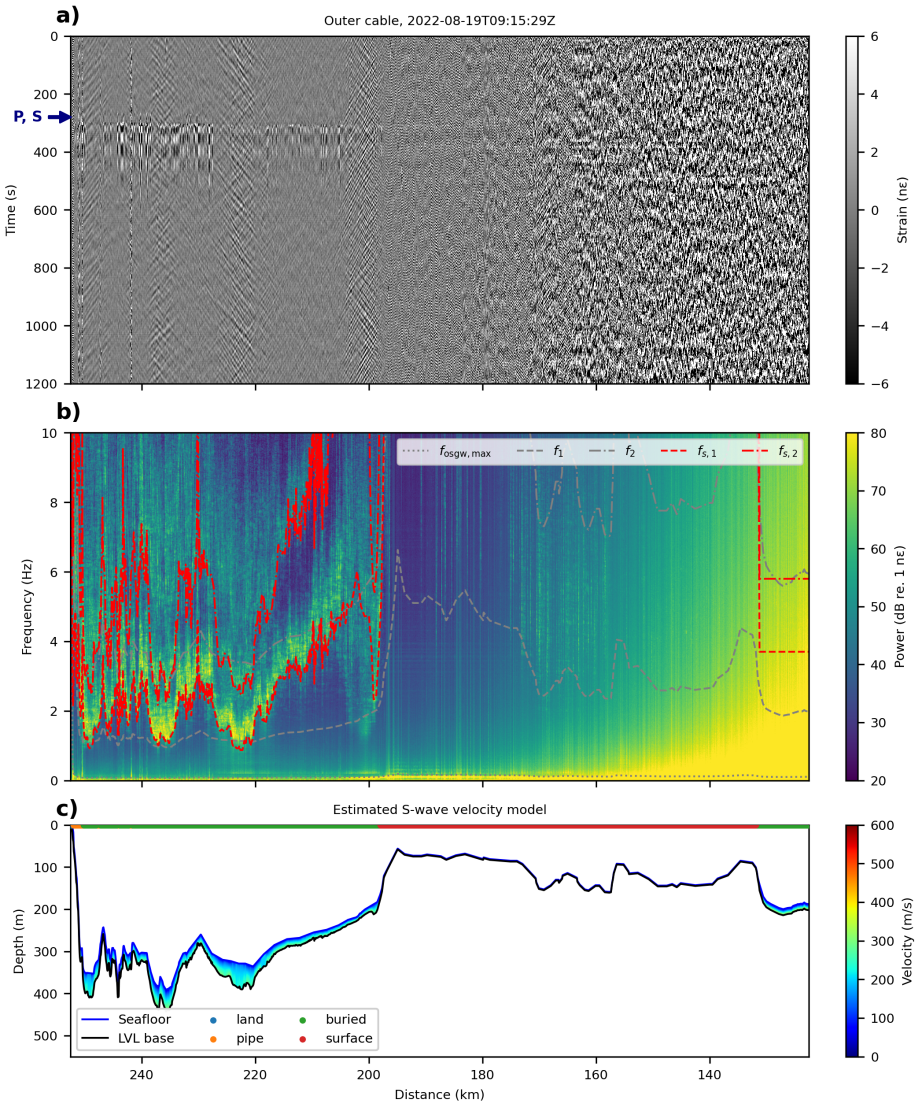

Figure 5: Frequency analysis of the DAS strain data with strong earthquakes recorded at 120 to 250 km distance of the outer cable by the interrogator in Ny-Ålesund. (a) The strain data in the 1200 s time window from 2022-08-19T09:15:29Z. (b) The f-x power spectra of the strain data in the 1200 s time window. (c) The structural depth profile below the sea level of the seafloor and the estimated LVL base, overlaid with the estimated S-wave velocity model of the LVL.

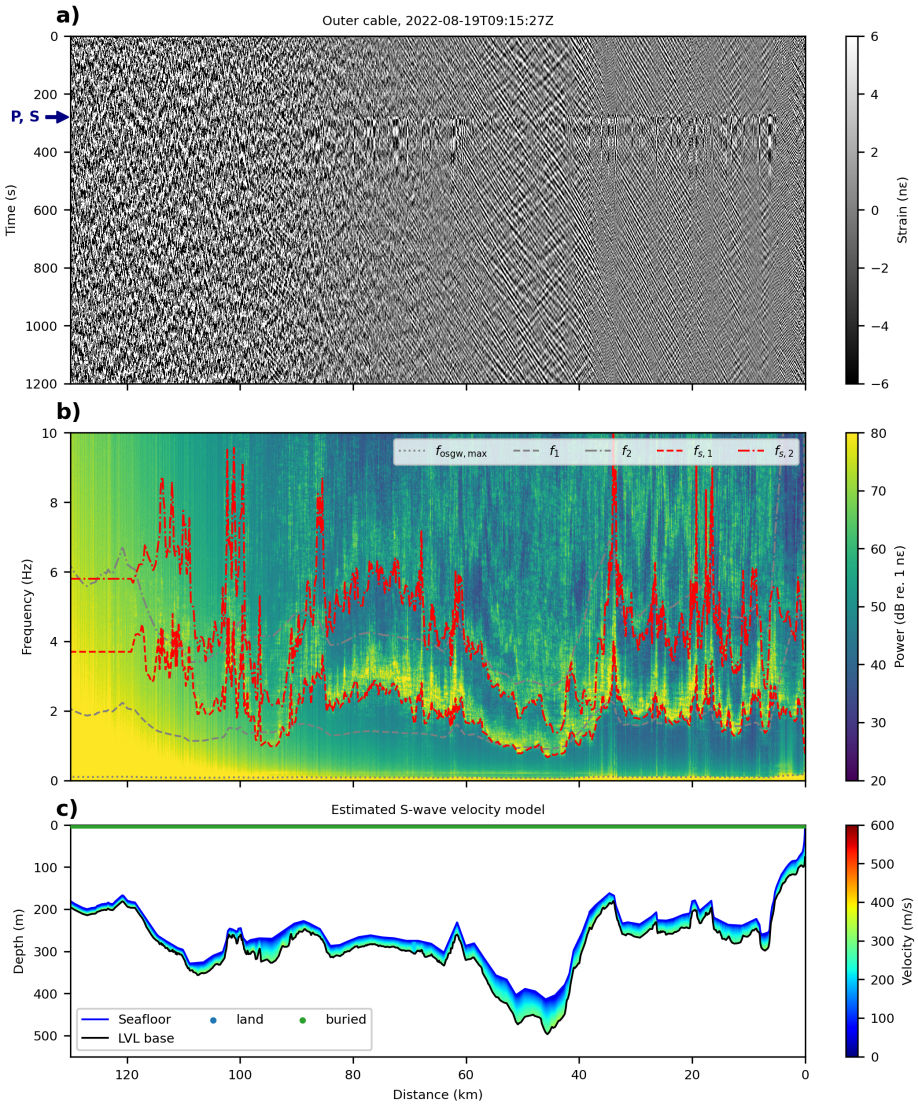

Figure 6: Frequency analysis of the DAS strain data with strong earthquakes recorded at 0 to 130 km distance of the outer cable by the interrogator in Longyearbyen. (a) The strain data in the 1200 s time window from 2022-08-19T09:15:27Z. (b) The f-x power spectra of the strain data in the 1200 s time window. (c) The structural depth profile below the sea level of the seafloor and the estimated LVL base, overlaid with the estimated S-wave velocity model of the LVL.

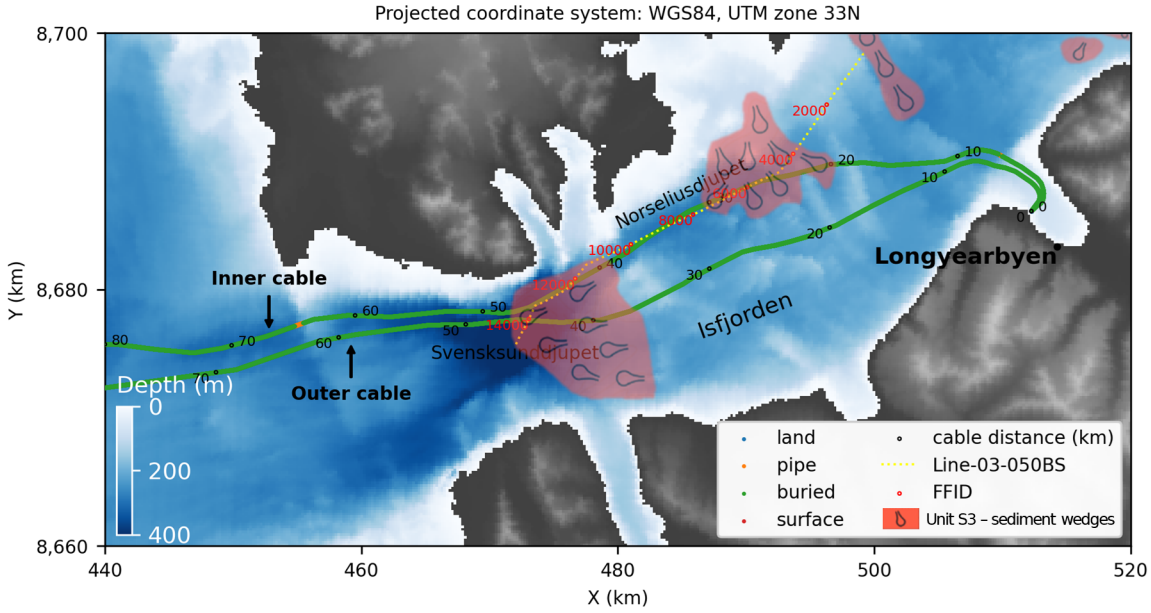

Figure 7: Enlarged map of the DAS arrays and the reference seismic data along the Isfjorden. The 2D seismic data "Line-03-050BS" is plotted and annotated with field file identifiers (FFIDs), namely, the shot numbers. The distribution of the sedimentary wedges (unit S3) reported in Figure 6B of Forwick and Vorren (2010) is also shown here. The map is referencing the projected coordinate system in Universal Transverse Mercator (UTM) Zone 33 North on WGS 84 (World Geodetic System 1984) geodetic coordinate reference system.

– **GEO-2023-0530.R2.accepted**

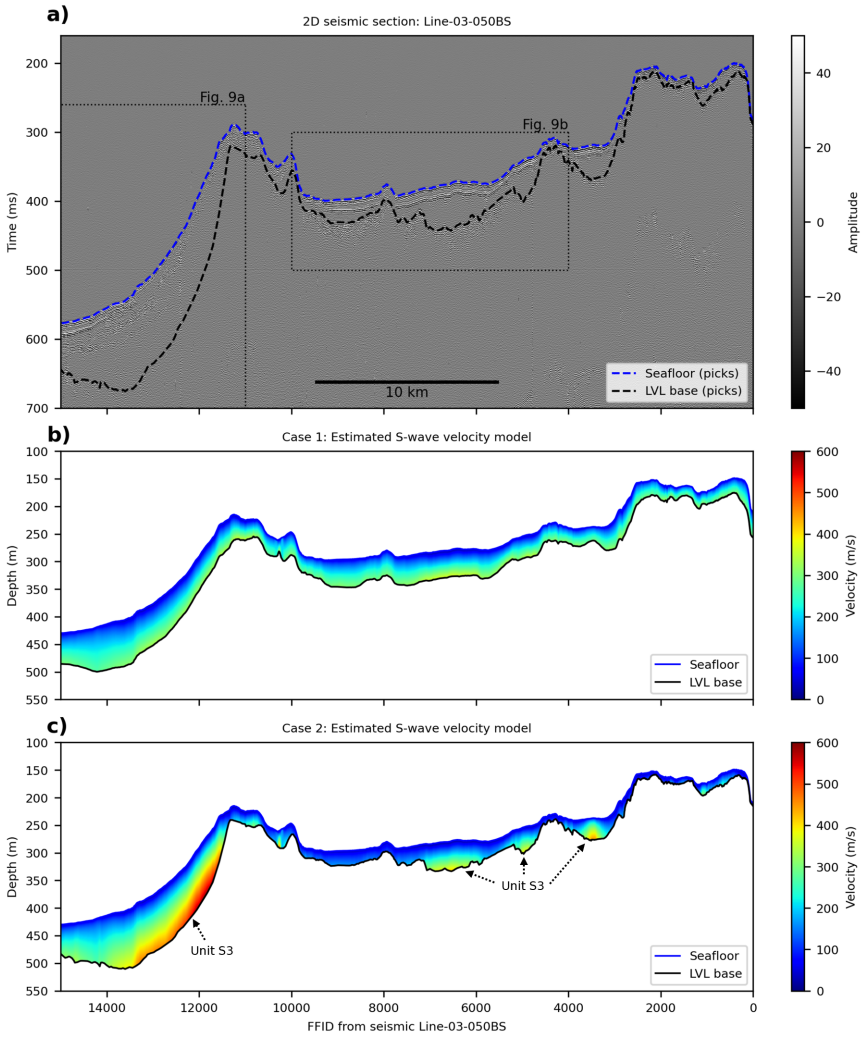

Figure 8: S-wave velocity models of the LVL. (a) The 2D seismic reflection data "Line-03-050BS" in the time domain overlaid with the interpreted seismic horizons of the seafloor and LVL base. The black dotted rectangles indicate the enlarged seismic sections shown in other figures. (b) The S-wave velocity model estimated in case 1 using only the DAS data (no other seismic data are involved). (c) The S-wave velocity model estimated in case 2, in which the LVL thickness is derived from the interpretation of the existing 2D seismic data shown in (a). The sedimentary wedges (unit S3) in the LVL are marked in (c) in correlation with their geographical distribution shown in Figure 7.

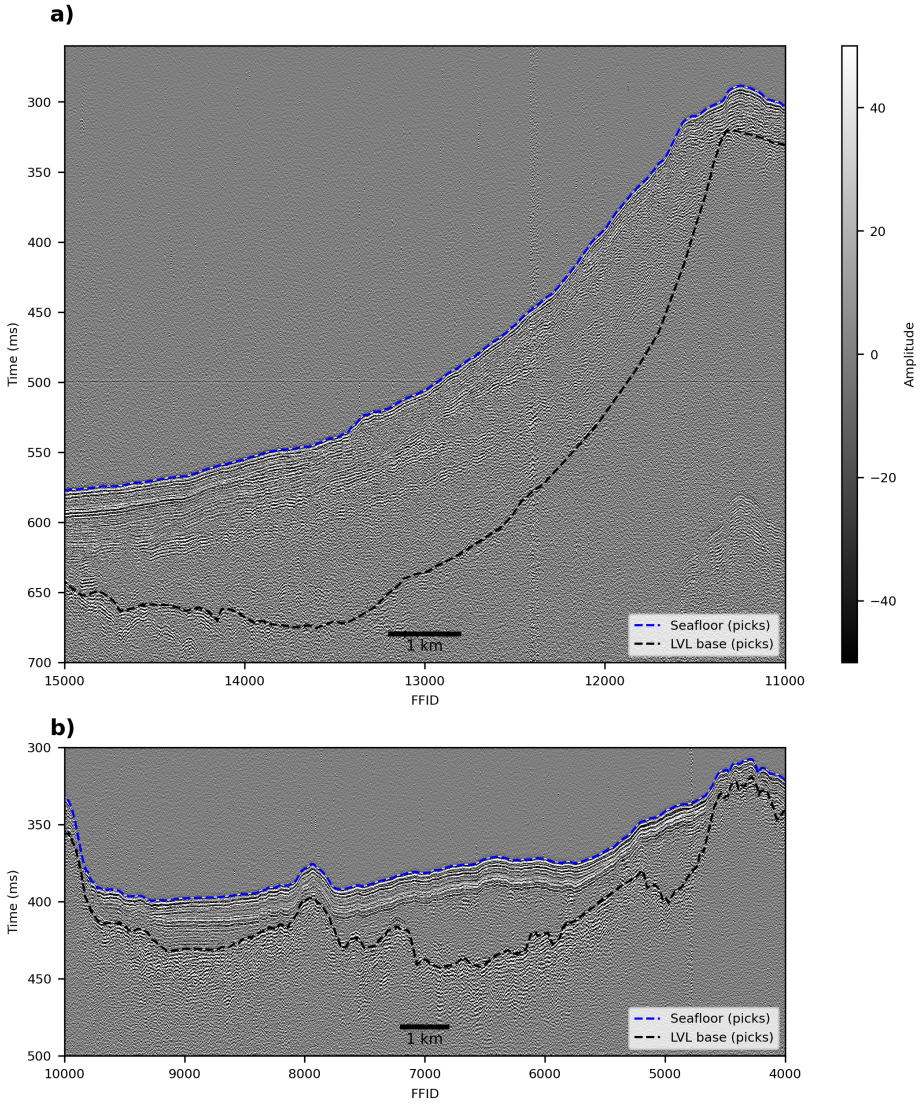

Figure 9: Enlarged 2D seismic sections in the rectangular regions shown in Figure 8a. (a) The section in Svensksunddjupet area. (b) The section in Norseliusdjupet area. A toponymic map presenting the key geographical locations in the Isfjorden area is shown in Figure 7.

– **GEO-2023-0530.R2.accepted**